Five-parameter characterization of intervariant boundaries in additively manufactured Ti-6Al-4V

N. Haghdadi [a,*], R. DeMott [a], P.L. Stephenson [a], X.Z. Liao [b,c], S.P. Ringer [b,c], S. Primig [a,*]

[a] School of Materials Science & Engineering, UNSW Sydney, NSW 2052, Australia
[b] Australian Centre for Microscopy & Microanalysis, The University of Sydney, NSW 2006, Australia
[c] School of Aerospace, Mechanical and Mechatronic Engineering, The University of Sydney, NSW 2006, Australia

HIGHLIGHTS

- 5-parameter crystallographic characteristics of boundaries in AM Ti-6Al-4 V were studied.
- Irrespective of the morphology, there is a strict Burgers OR between α and β.
- AM Ti-6Al-4V microstructures show a maximum population of prismatic planes.
- The crystallographic constraints imposed by the BOR determine the plane characteristics.

GRAPHICAL ABSTRACT
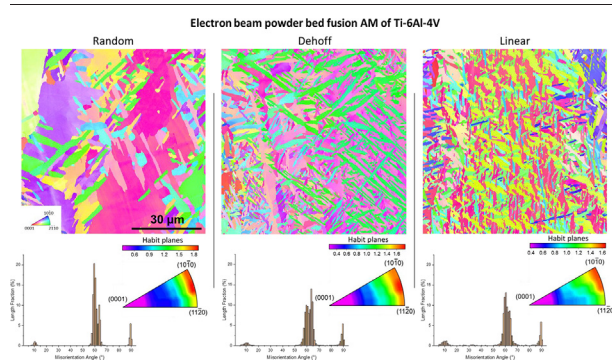
ABSTRACT

Additive manufacturing has emerged as a promising route to fabricate complex-shaped Ti-6Al-4V parts. The microstructural evolution and variant selection across builds in response to different printing strategies processed by electron beam powder bed fusion has been previously clarified. However, a detailed knowledge of the grain boundary plane characteristics of the α-α intervariant interfaces is still missing. The aim of this study was to reveal the full 'five-parameter' crystallographic characteristics of the intervariant boundaries. The most common α-α intervariant for colony and basketweave microstructures was 60°/[1 1 $\overline{2}$ 0], while in the acicular microstructure, the maximum was at 63.26°/[$\overline{10}$ 5 5 $\overline{3}$]. This is discussed in terms of self-accommodation during the β to α phase transformation, and the degree of coherence of the α laths in the as-deposited condition and during further growth. The grain boundary plane distributions reveal a high tendency for intervariant boundaries to terminate on prismatic and pyramidal planes rather than on low-energy basal planes. This suggests that, during additive manufacturing of Ti-6Al-4V and irrespective of the α morphology, the crystallographic constraints imposed by the Burgers orientation relationship determine the boundary plane distribution characteristics.

© 2020 The Author(s). Published by Elsevier Ltd. This is an open access article under the CC BY-NC-ND license (http://creativecommons.org/licenses/by-nc-nd/4.0/).

1. Introduction

Ti-6Al-4V is currently the most commonly used titanium alloy with a wide range of applications in industries such as aerospace, defence, biomedical, and maritime [1]. There are intense and ongoing efforts to enhance the properties and performance of this alloy via cost-effective manufacturing routes [2]. The most recent revolution in Ti-6Al-4V manufacturing has been the emergence of additive manufacturing

* Corresponding authors at: School of Materials Science & Engineering, UNSW Sydney, NSW 2052, Australia.
E-mail addresses: nima.haghdadi@unsw.edu.au (N. Haghdadi), s.primig@unsw.edu.au (S. Primig).

(AM), also known as 3D printing [3]. Ti-6Al-4V is a pioneer alloy in the successful adoption of AM for manufacturing of metallic products. There are a number of different AM techniques capable of processing this alloy [3]. However, electron beam powder bed fusion (EPBF) is the ideal technique for fabricating oxygen-free Ti-6Al-4V parts because it can be conducted in a vacuum chamber [4]. During EPBF, a high energy electron beam is used to melt and bind together metallic powder feedstock [5]. Generally, metals go through complex thermal cycles during AM, resulting in severe thermal gradients and gyrations within the parts, significantly different from typical thermal profiles during conventional manufacturing [6]. While some of the fundamentals of AM can be understood based on the concepts already established for welding [7], the complexity of relationships between AM processing parameters and microstructure of AM products [8] underpins the need for a detailed processing-structure-performance study.

During EPBF, Ti-6Al-4V first solidifies as the body centred cubic (BCC) β phase. As Al and V provide negligible constitutional supercooling [9], the driving force for nucleation is low, and thus, β grains are usually coarse and columnar. The β then transforms to the hexagonal close-packed (HCP) martensitic α' phase, since the cooling rate during EPBF exceeds 410 Ks^{-1} [10]. Upon deposition of the subsequent layers, α' will decompose into the HCP α phase and a low fraction of the β phase [11]. It has been reported that both α' and α follow the so-called Burgers orientation relationship (OR) with β, i.e., $\{110\}_{\beta}//\{0001\}_{\alpha}$ and $\langle 111 \rangle_{\beta}//<11\overline{2}0>_{\alpha}$, or equivalently 45.3^0/[26 1 3] [12]. According to the Burgers OR, each β orientation can transform into 12 distinct α variants [12]. The preferred formation of selected variants ('variant selection') and the preferential arrangements of variants with regards to each other have been studied extensively in conventionally manufactured Ti-6Al-4V [13] and pure Ti [14]. The underlying mechanisms reported are governed by phase transformation constraints, transformation energy, β boundaries characteristics, and external strain energy [13–17]. In the case of AM, however, there are only limited studies on variant selection [18,19]. Our previous work has revealed that prior β grain boundary characteristics and strain accommodation during BCC to HCP phase transformation play major roles in variant selection of EPBF Ti-6Al-4V, and a change in printing strategy or position along the build height will change the dominant mechanism [19]. That study focused on orientation of α grains and texture measured using 2D EBSD which does not provide full insights into the characteristics of intervariant boundaries including the interfacial planes.

The boundary plane character has been shown to govern the energy of the boundary and play an important role in a number of phenomena such as interface precipitation and slip transfer [20–22]. In Ti alloys, the character of α-α boundaries affects their mechanical properties because the extent of dislocation slip transmission depends on the α boundary characteristics. For example, $\{1\,0\,1\,2\}$ twin boundaries transmit basal dislocations under sufficiently high stresses [21], while $\{1\,0\,1\,1\}$ twin boundaries act as barriers to the basal slip of dislocations [22]. Phase transformations and thermomechanical processing are the most significant factors in determining the character of such interfaces [24]. Since Ti-6Al-4V goes through complicated phase transformations and thermal cycles during AM, a full characterization of intervariant boundaries as a function of AM strategy can guide the optimisation of AM parameters to achieve the properties of interest. To the best of our knowledge, there has been no study on the thorough crystallographic characteristics of intervariant boundaries in AM Ti-6Al-4V, including the characterization of boundary planes.

Studies of the complete characteristics of the crystallography of interfaces require five independent crystallographic parameters e.g., three 'Euler' angles defining the lattice misorientation as well as boundary trace and plane normal defining the habit plane [25]. Only four of these can be readily accessed by a standard electron back scatter diffraction (EBSD) measurements, because the plane normal is unavailable. Methods such as 3D-EBSD, transmission electron microscopy or

advanced X-ray diffraction can be used to characterize interface planes [26–28]. Despite their usefulness, all of these methods are highly time consuming and usually only characterize a few boundaries at a time. Due to this limitation, the full five-parameter grain boundary character distribution (GBCD) is rarely reported for bulk materials despite the importance of the plane character in determining the properties of interfaces. An alternative method based on a stereological analysis of interface traces in 2D EBSD data has been recently put forward to identify the plane distribution in different materials [25], showing an excellent agreement with corresponding 3D measurements. While this method has been used to characterize the distribution of grain boundaries in Ti-6Al-4V and pure Ti processed by conventional processing [14, 28–30], no work has been reported on a thorough characterization of intervariant boundaries in AM Ti-6Al-4V microstructures. This is the focus of the current study.

This study reveals how thermal variations as a result of scanning strategy and distance from the substrate affects the five parameter crystallographic characteristics of α-α intervariant boundaries in EPBF Ti-6Al-4V. A full characterization of intervariant boundaries as a function of AM processing parameters will provide new insights into how grain boundaries can be favourably manipulated through optimizing AM processes.

2. Experimental

Three Ti-6Al-4V builds with dimensions of 15 × 15 × 25 mm^3 (xyz) were printed at the Oak-Ridge National Laboratory, USA. The chemical composition of the powder was 6.14 Al, 4.03 V, 0.13 Fe, 0.06 O, 0.01 N, 0.01C, balance Ti (wt%). An ARCAM Q10 plus electron beam powder bed fusion machine was used with a build temperature of 470 °C and a vacuum pressure of ~3.3 × 10^{-2} Torr. Three scanning strategies, 'random', 'linear', and 'Dehoff' (Fig. 1) were applied using a layer thickness of 50 μm and a current of 11 mA. In the random strategy, each point on a layer is chosen randomly, such that it experiences an equal probability of being melted [32]. The Dehoff point fill is a special type of linear fill where only every eleventh point is filled, further details are given elsewhere [33]. The linear strategy scans the electron beam back and forth along the powder bed with 67.5° rotation between layers. Microstructure observation and grain boundary character distribution (GBCD) analysis was carried out on the ZX surfaces in three distinct regions of 'bottom' (~1 mm from the base plate), 'middle' (~12.5 mm from the base plate), and 'top' (~24 mm from the base plate). Samples for EBSD were prepared using mechanical grinding and polishing followed by mechanochemical polishing using a 0.04 μm colloidal silica OPU/7.5% H$_2$O$_2$ solution.

Extensive EBSD analysis of the samples was carried out using a JEOL 7001F field emission scanning electron microscope equipped with a Hikari 31 Super EBSD Camera. Orientation data were collected using an accelerating voltage of 25 kV, working distance of ~15 mm, 6 × 6 binning, a hexagonal grid, and a step size of 0.3 μm. Post-processing of EBSD data was carried out via the OIM Analysis v8 software. Multiple scans were carried out to ensure collection of data of more than 200,000 boundary segments for each of the microstructures. The collected EBSD maps were subjected to three steps of cleaning before extracting the boundary segments including: (1) Iterative grain dilation cleaning with a minimum of 5 pixels grain size, (2) assignment of a single average orientation to each individual grain using 5° of tolerance angle, and (3) dividing curved grain boundaries connecting two triple points into linear segments with a boundary deviation limit of 2 pixels (i.e. 0.6 μm). It has to be noted that the α' and α phases both have HCP crystal structures with similar lattice parameters, therefore they cannot be differentiated by EBSD [34]. Although the β phase does occur in the EPBF Ti-6Al-4V samples, it only appears along limited boundaries on a fine scale lower than the resolution limit of EBSD. Since the study of β phase character is outside of the scope of this study, only the α phase (or α') was indexed.
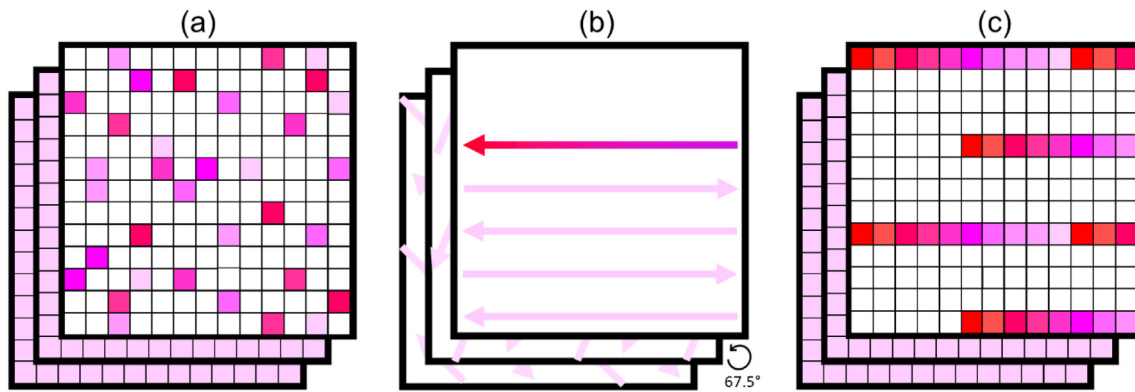
Fig. 1. Graphical representations of the (a) random point fill, (b) linear raster, and (c) Dehoff point fill scans.

The extracted boundary segments were used to calculate the grain boundary plane distribution at different grain boundary misorientations. This was done using the automated stereological methodology developed by Rohrer et al. [25]. This method is based on a statistical trace analysis of boundaries with special misorientation angles/axes. A full description of the method has been given in [25]. Once the plane normal is measured, one can classify the character of boundaries e.g., as tilt, twist, and symmetric. A boundary is a tilt boundary if its plane normal is perpendicular to the misorientation axis, a twist boundary if its plane normal is parallelpp to the misorientation axis, and a symmetric boundary if its plane is a mirror between crystal structures separated by the boundary [35].

To reconstruct prior β grains, the software and methodology developed by Davies et al. [36] were employed. This software detects α variants, calculates their potential β parent orientations and compares the results with neighbouring variant solutions to determine a single unique solution. This software needs two input variables, i.e., maximum misorientation angle between two points to be considered part of the same α variant and the maximum deviation from the Burgers orientation relationship [36]. Based on the optimisations in [37], these variables were chosen as 2° and 3°, respectively.

3. Results

Fig. 2 shows an overview of the microstructure of the EPBF Ti-6Al-4V alloy as a function of scanning strategy and build height in inverse pole figure (IPF) colouring. It is observed that the α laths are very diverse in terms of size, morphology, and orientation across the build height for different scanning strategies. Grain boundary α (GBα) is observed along some of the prior β grain boundaries. There are cases where α laths grow directly from the grain boundaries into the interior of the parent β grains rather than along the grain boundary. There are also interior α laths without any obvious connection to the prior β grain boundaries. These may have formed heterogeneously on intragranular inclusions, dislocations or low angle grain boundaries, or alternatively through sympathetic nucleation on existing α laths. A more detailed understanding of these features would require 3D EBSD.

The microstructures resulting from the random scan strategy consist of relatively coarse α sheaves with similar orientations separated by low angle boundaries, a characteristic of a colony-type microstructure. Such colonies are observed across the height of the build. In the linear fill microstructures, α laths adopt an interwoven Widmanstätten morphology, creating a basketweave structure. The microstructure is consistent across the build height. In contrast to the linear and random fill strategies, the Dehoff fill resulted in the most significant local differences in the morphology across the height of the samples. Top and middle parts of the Dehoff build show a mixture of basketweave and colony α morphologies, while much finer α laths are observed in the bottom

map. This fine, acicular morphology is not highly interwoven but instead resembles a martensitic microstructure.

Distinct microstructures formed across the build height for different scanning strategies correspond to the rate of β to α transformation that each region experiences during the late stages of the EPBF process. The evolution of microstructure during EPBF of Ti-6Al-4V has been previously studied [38]. After initial solidification, EPBF can be considered as a pseudo-isothermal heat treatment at the build pre-heat temperature, superimposed by thermal fluctuations from subsequent layers. Al-Bermani et al. [38] have shown that each part of material may liquify and solidify ~ three times during EBPF, followed by several cycles through the β transus temperature. These thermal cycles can result in the decomposition of α' to different α morphologies. Such an evolution of the microstructure has been experimentally confirmed by Sridharan et al. [18], where the martensitic first layer of Ti-6Al-4V decomposed to a basketweave and colony microstructure by deposition of a fourth layer.

The slowest cooling rate results in a lamellar microstructure with a colony morphology (Fig. 2). The colonies, i.e., clusters of parallel α plates that belong to a single crystallographic variant, first form along the β grain boundaries. Using phase field modelling, Wang et al. [39] have shown that colony microstructures can develop from the grain boundary via an interface instability mechanism. Upon an increase in the cooling rate, fully lamellar structures are replaced with fine α plates (Fig. 2). As the cooling rate increases, smaller individual α grains nucleate at the grain boundaries. Moreover, a high cooling rate increases the rate of intragranular (e.g., on defects such as dislocations), sympathetic (on an existing α plate) [40], and coherency stress induced (i.e. auto-catalytic effect) [41] nucleation. This results in a finer colony size and a Widmanstätten α morphology, creating an interwoven basketweave structure. A mixture of colony and basketweave microstructural features can be achieved at moderate cooling rates. The other characteristic microstructure observed in the current study with a high morphological similarity to martensitic microstructures is observed in the Dehoff bottom sample, with an acicular morphology where plates are not highly interwoven. The detailed mechanism behind the formation of such structures in the Dehoff bottom sample is not clear yet and needs further in-depth study through a site-specific thermal gradient measurement within the samples during EPBF. This is beyond the scope of the current study.

Further analyses are carried out on four different representative types of microstructures observed, i.e. random top (colony), linear top (basketweave), Dehoff middle (mixed: mixture of colony and basketweave), and Dehoff bottom (acicular) to elucidate how different morphologies of α can affect five-parameter intervariant boundary characteristics. The misorientation histogram for the α-α boundaries displays multiple peaks (Fig. 3). For all microstructures studied, the most significant peaks appear at misorientation angles of ~10°, 55–65°
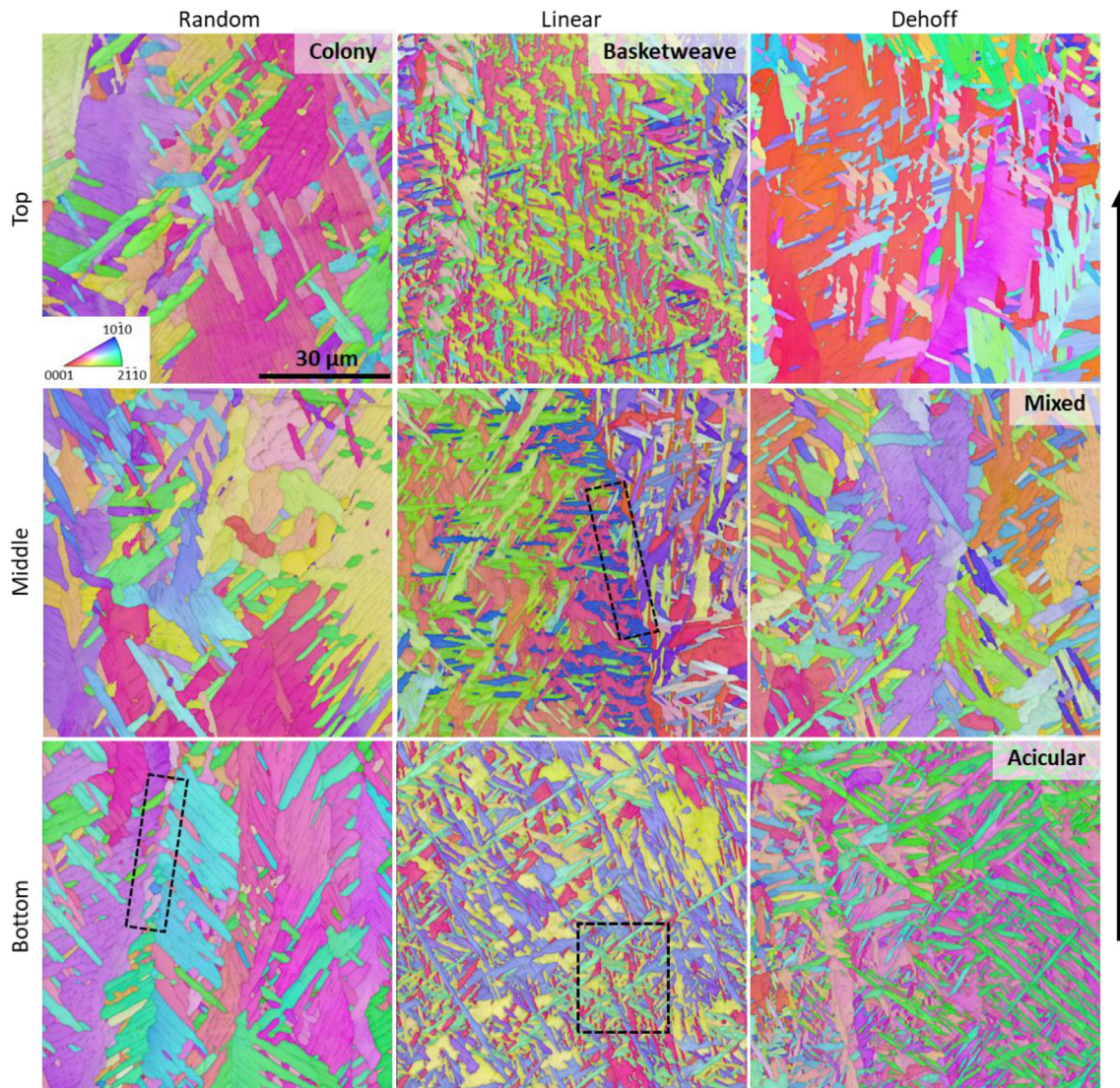
Fig. 2. IPF colour maps (along the build direction) of the specimens differing in build height and scanning strategy. The arrow shows the build direction (z-axis). The selected microstructures for in-depth study are labelled. Dashed rectangles in Random Bottom, Linear Middle, and Linear Bottom microstructures show examples of Grain boundary α, growth of α laths from the grain boundaries into the interior of the parent β grains, and interior α laths without any obvious connection to the prior β grain boundaries, respectively.

and ~90°. This is different to what is expected from a random (Mackenzie) misorientation angle distribution between HCP grains [30]. The misorientation axes corresponding to each of these misorientation angle peaks is clustered at specific axes. According to the Burgers OR, each β orientation can create twelve distinct α variants (Table 1). The impingement of these variants with each other creates five distinct misorientation angle/axis pairs associated with these boundaries (Table 1). Both the angles and axes of all the peaks in Fig. 3 correspond well with these five unique misorientations. This shows that irrespective of the type of the microstructure formed, the β to α (α') phase transformation during EPBF of Ti-6Al-4 V occurs following the Burgers OR.

Using a 2° deviation from the ideal misorientation angle/axis, the length fraction of different types of intervariant boundaries for different microstructures are plotted in Fig. 4. The theoretical length fraction of each of these boundaries, based on the assumption that all 12 variants nucleate and grow equivalently (assuming no α-α impingement at prior β grain boundaries), is also included. The results show that the intervariant boundary distribution deviates largely from the theoretical values, consistently across all morphologies. Moreover, there is a difference in the

length fraction of each boundary across different microstructures. In the colony and basketweave type microstructures, 60°/[1 1 $\overline{2}$ 0] is the most common boundary, while 63.26°/[$\overline{10}$ 5 5 $\overline{3}$] is the most frequent intervariant boundary in the acicular (Dehoff bottom) microstructure. The colony structure shows a higher fraction of 60.83°/[$\overline{10}$ $\overline{7}$ 17 3] and 10.53°/[0 0 0 1] boundaries than the basketweave or acicular structures. Furthermore, the colony microstructure possesses the highest fraction of the boundaries that do not correspond to any of the Burgers OR related misorientations.

The distribution of boundary planes for all the intervariant boundaries, irrespective of misorientation (Fig. 5), shows a high anisotropy in microstructures with a maximum intensity of ~1.7–1.9 multiple random distribution (MRD) at the prismatic {h k i 0} planes. Here, a MRD of 1.7 means the population of these planes is ~70% higher than random distribution. The minimum population is ~0.3–0.4 MRD at the {0001} basal plane. An intermediate population of planes can be observed at pyramidal planes with peaks of ~1.2 MRD close to the (1 0 $\overline{1}$ 1) planes. The acicular microstructure shows the sharpest peak at (4 1 $\overline{5}$ 0),
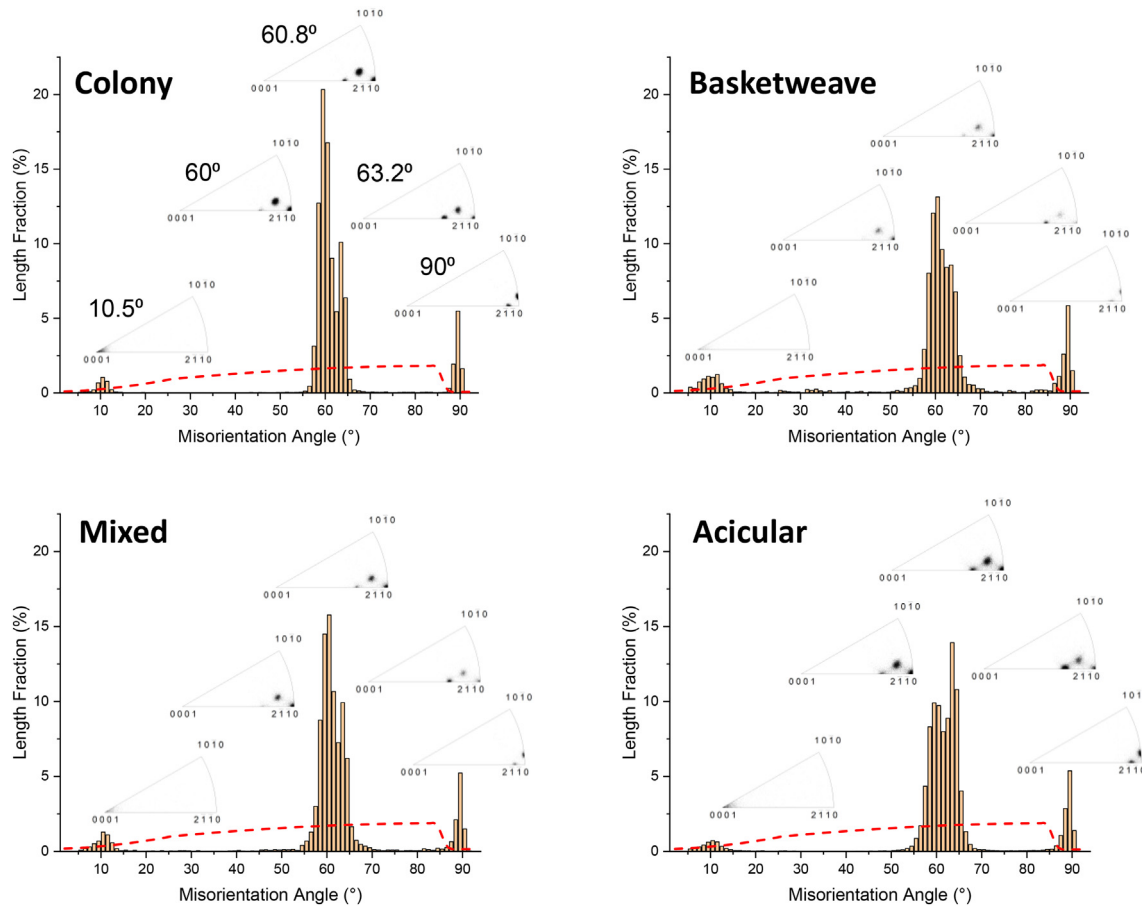
Fig. 3. The misorientation angle distribution of α-α boundaries along with misorientation axes for specific misorientation angles associated with the Burgers OR for different characteristic microstructure types. The dashed lines represent the random (Mackenzie) misorientation angle distribution between HCP grains.

spreading towards (1 0 $\bar{1}$ 0) and (1 1 $\bar{2}$ 0) planes. Basketweave, colony and mixed microstructures all show clusters of planes at around (4 1 $\bar{5}$ 0), spreading towards (1 0 $\bar{1}$ 0).

The plane character was examined for all microstructures for the peaks observed in the misorientation distribution, corresponding to intervariant boundaries. The distribution of planes is presented in Fig. 6. The theoretical position of characteristic grain boundaries has also been included (plotted using the grain boundary toolbox software by Glowinski [42]). The overall view implies that the plane distribution is anisotropic, and that the position of planes is highly dependent on the misorientation, thus, intervariant boundary type. However, except for the 10.53°/[0 0 0 1] boundaries, the plane character seems fairly independent of the microstructure type or, more generally, printing

Table 1
Possible α variants produced through the β → α phase transformation through the Burgers orientation relationship and resultant α-α intervariant boundaries [13].

Variant	Planes parallelism	Directions parallelism	Rotation angle/axis from V1
V1	$(1\bar{1}0)_\beta\|(0001)_\alpha$	$[111]_\beta\|[11\bar{2}0]_\alpha$	–
V2	$(10\bar{1})_\beta\|(0001)_\alpha$	$[111]_\beta\|[11\bar{2}0]_\alpha$	60°/[1 1 $\bar{2}$ 0]
V3	$(01\bar{1})_\beta\|(0001)_\alpha$	$[111]_\beta\|[11\bar{2}0]_\alpha$	60°/[1 1 $\bar{2}$ 0]
V4	$(110)_\beta\|(0001)_\alpha$	$[1\bar{1}1]_\beta\|[11\bar{2}0]_\alpha$	90°/[1 $\bar{2.38}$ 1.38 0]
V5	$(101)_\beta\|(0001)_\alpha$	$[1\bar{1}1]_\beta\|[11\bar{2}0]_\alpha$	63.26°/[$\bar{1}0$ 5 5 $\bar{3}$]
V6	$(01\bar{1})_\beta\|(0001)_\alpha$	$[1\bar{1}1]_\beta\|[11\bar{2}0]_\alpha$	60.83°/[$\bar{1.377}$ $\bar{1}$ 2.377 0.359]
V7	$(110)_\beta\|(0001)_\alpha$	$[11\bar{1}]_\beta\|[11\bar{2}0]_\alpha$	90°/[1 $\bar{2.38}$ 1.38 0]
V8	$(10\bar{1})_\beta\|(0001)_\alpha$	$[11\bar{1}]_\beta\|[11\bar{2}0]_\alpha$	60.83°/[$\bar{1.377}$ $\bar{1}$ 2.377 0.359]
V9	$(011)_\beta\|(0001)_\alpha$	$[11\bar{1}]_\beta\|[11\bar{2}0]_\alpha$	63.26°/[$\bar{1}0$ 5 5 $\bar{3}$]
V10	$(1\bar{1}0)_\beta\|(0001)_\alpha$	$[11\bar{1}]_\beta\|[11\bar{2}0]_\alpha$	10.53°/[0 0 0 1]
V11	$(101)_\beta\|(0001)_\alpha$	$[11\bar{1}]_\beta\|[11\bar{2}0]_\alpha$	60.83°/[$\bar{1.377}$ $\bar{1}$ 2.377 0.359]
V12	$(011)_\beta\|(0001)_\alpha$	$[11\bar{1}]_\beta\|[11\bar{2}0]_\alpha$	60.83°/[$\bar{1.377}$ $\bar{1}$ 2.377 0.359]

condition. The population of planes at the peaks, however, changes across diverse microstructures. For all microstructures, the grain boundary plane distribution for the 10.53°/[0 0 0 1] misorientation is noisy and has maxima lower than 0.3 MRD. Thus, this was not considered significant for more in-depth studies. The grain boundary plane distribution for 60°/[1 1 $\bar{2}$ 0] shows a peak close to the pyramidal ($\bar{1}$ 1 0 1) plane for all microstructures studied. The colony microstructure had the
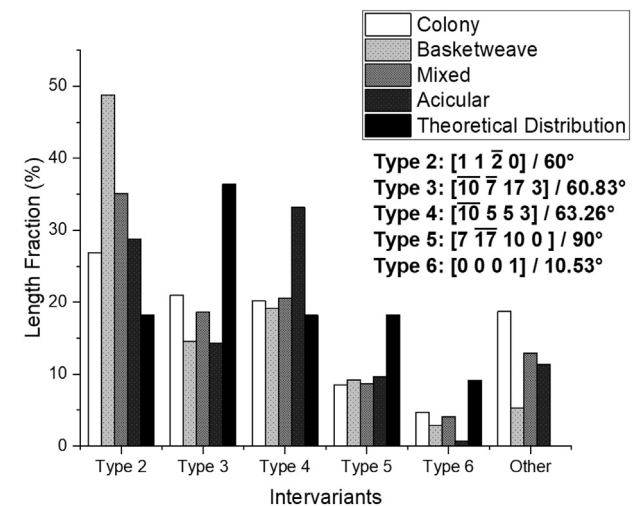
Fig. 4. Length fraction of intervariant boundaries associated with the Burgers OR for different microstructures along with the theoretical length fraction under random nucleation and growth assumption.
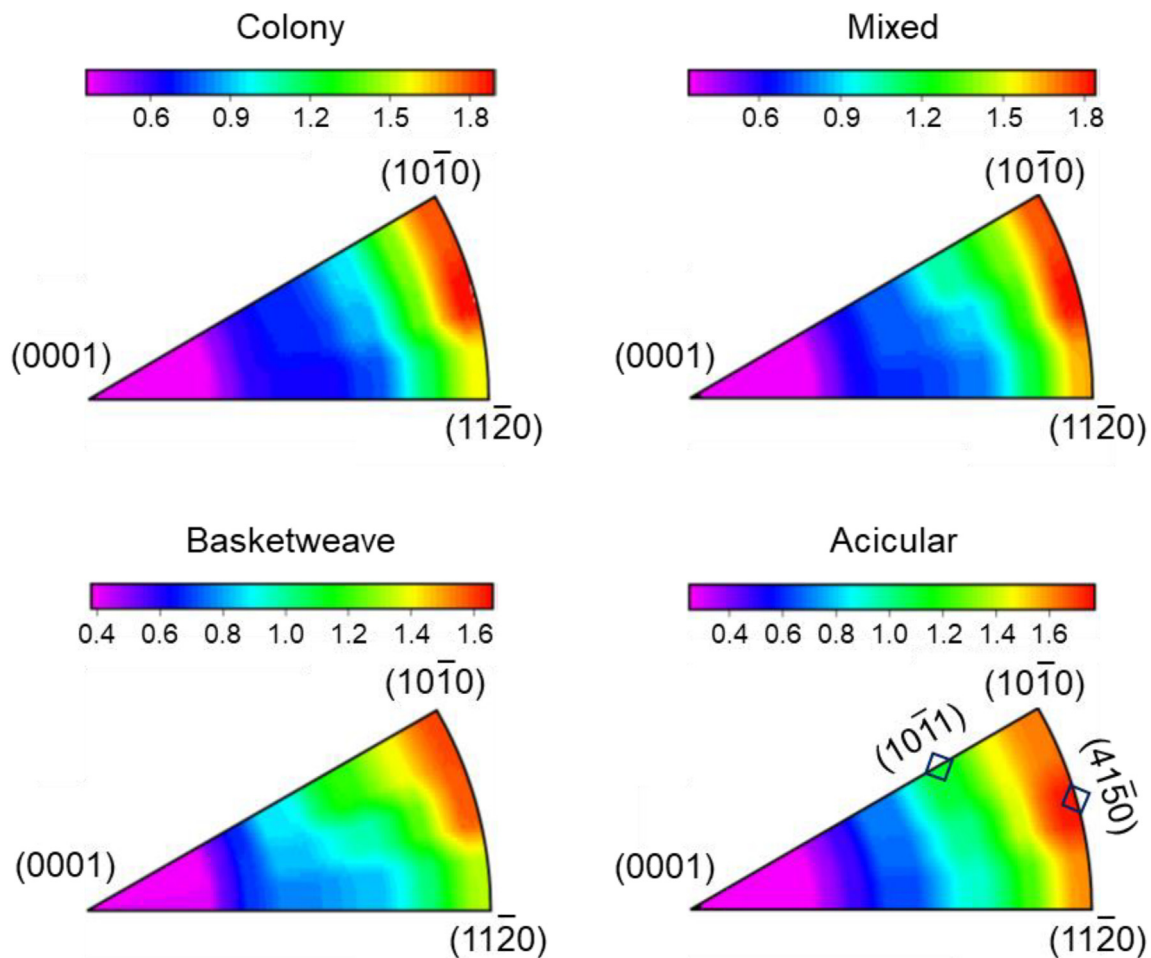
Fig. 5. 2-D distribution of α-α intervariant boundaries planes for all misorientations in different microstructures. The scale is in multiple random distribution (MRD).

most diffuse peak, with an intensity of ~230 MRD. The ($\bar{1}$ 1 0 1) plane is very close to the ($\overline{15}$ 15 0 16) plane, which would result in a twist/symmetric tilt boundary.

The distribution of boundary planes for the 60.83°/[$\overline{107}$ 17 3] intervariant boundary reveals a peak near (1 1 $\bar{2}$ 0) planes for all microstructures (Fig. 6). This boundary is close to (13 19 32 3) which has a twist character. Interestingly, the population of planes is highest for the acicular structure, followed by colony microstructure, mixed microstructure, and the basketweave microstructure. 63.26°/[$\overline{10}$ 5 5 $\bar{3}$] intervariant boundaries mostly terminate on planes around the ($\bar{7}$ 5 2 1) plane, which is very close to the ($\bar{3}$ 2 1 0) twist boundary plane. The highest population of these planes is observed for the acicular structure followed by the mixed and colony microstructures, and the basketweave microstructure. The intervariant plane distribution for the 90°/[7 $\overline{17}$ 10 0] reveals a diffuse peak close to the (15 $\overline{15}$ 0 16) plane for all of microstructures. The plane intensity for this boundary is ~ 36, 33, 25 and 24 MRD for the colony, mixed, basketweave, and acicular microstructures, respectively.

4. Discussion

The intervariant boundaries distribution analysis shows that in all EPBF microstructures five distinct characteristic misorientations are found, all of which are associated with the Burgers OR. In all of the microstructures except the acicular one, the 60°/[1 1 $\bar{2}$ 0] boundaries are the most common intervariant boundaries (Fig. 4), occasionally

demonstrating a triangular morphology (Fig. 7). A high population of these boundaries have been observed in previous studies [13,14] in martensitic transformation in pure Ti, which has been ascribed to the so called 'self-accommodation' phenomenon. According to the phenomenological theory of martensite, the BCC to HCP martensitic transformation in Ti alloys is accompanied by shear and dilatational shape strain elements. Wang et al. [13] suggested that formation of 60°/[1 1 $\bar{2}$ 0] and 63.26°/[$\overline{10}$ 5 5 $\bar{3}$] intervariant boundaries would minimize the shear shape strain. Complementary studies by Farabi et al. [14] demonstrated that 60°/[1 1 $\bar{2}$ 0] is the preferential intervariant boundary once minimization of both dilation and shear components was considered, provided that the martensitic phase transformation was accommodated by slip but not twinning.

Based on shape and spatial orientation independent (non-configurational) elastic interaction energy minimization, Balachandran et al. [43] have shown that 63.26°/[$\overline{10}$ 5 5 $\bar{3}$] and 60°/[1 1 $\bar{2}$ 0] are the preferred intervariant boundaries for coherent and semi-coherent α laths, respectively. The dominance of 60°/[1 1 $\bar{2}$ 0] boundaries suggests that the α phase in the colony, basketweave and mixed microstructures most likely loses its coherency during the growth process. There have been also suggestions that the three variants could nucleate autocatalytically as a result of the elastic interactions between new coherent nuclei and semi-coherent precipitates, forming a pyramid [43]. It is noted that there are also cases in the microstructure where 2-variant clusters of 60°/ [1 1 $\bar{2}$ 0] boundaries are observed instead of 3-variant clusters (see Fig. 7). As the minimum equivalent strain associated with such configurations is about 10 times higher than 3-variant clusters [14], this is
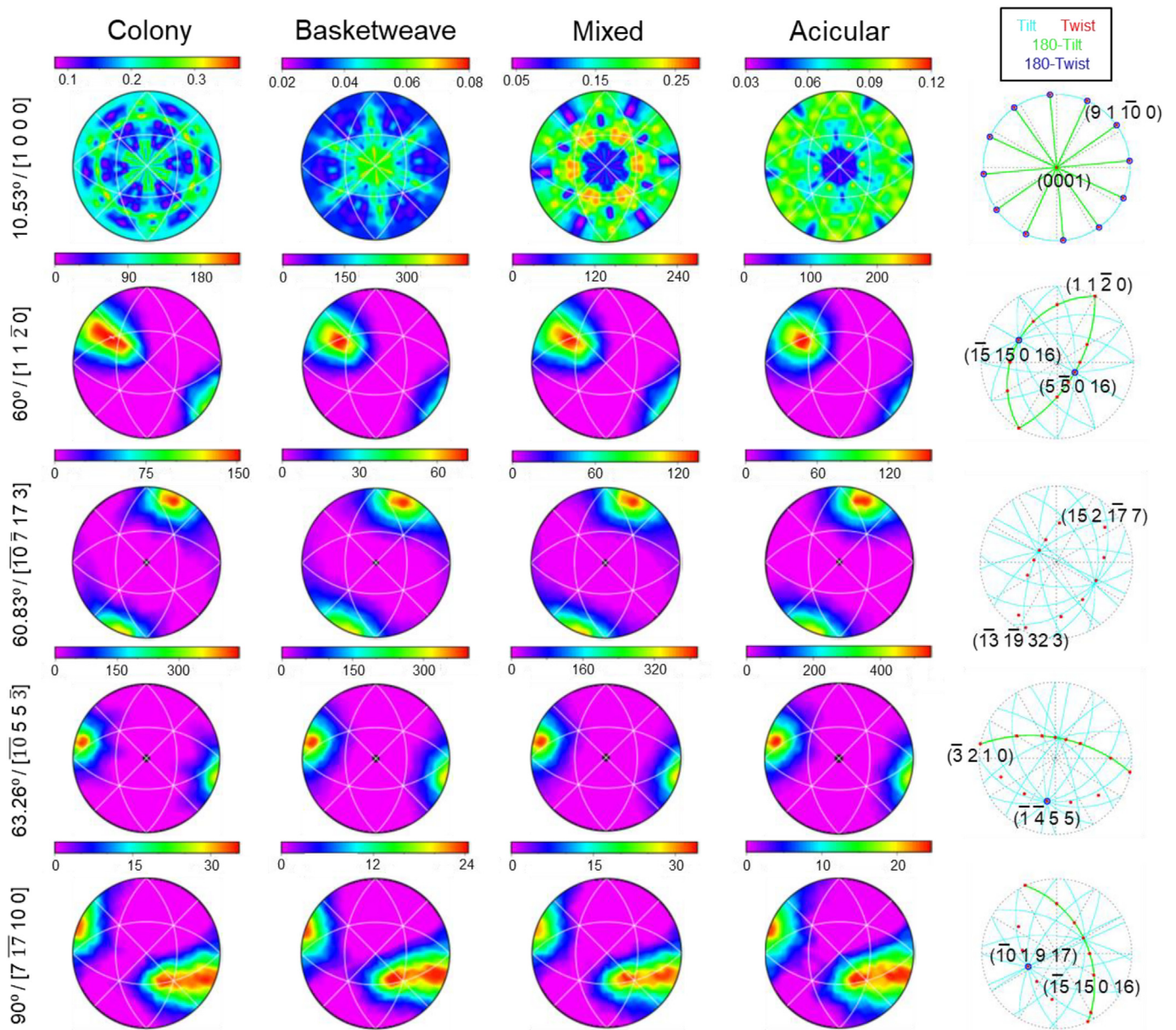
Fig. 6. Distribution of intervariant boundary planes for different misorientations associated with the Burgers OR in different microstructures. Scale bars are in MRD. The geometrically characteristic boundaries corresponding to each misorientation is plotted for reference.
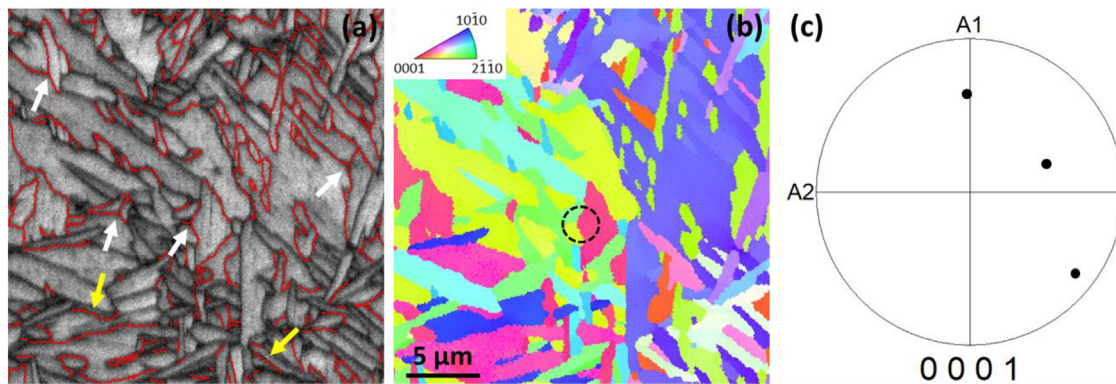

Fig. 7. (a) Image quality map with red lines denoting 60°/[1 1 2̄ 0] inter-variant boundaries and (b) the corresponding IPF map. Examples of 60°/[1 1 2̄ 0] triangular and lines are shown by white and yellow arrows, respectively. (c) (0001) pole figure plots with three α grains making up the dashed cluster in (b).

likely just the result of a sectioning effect where only two of the three variants lie in the plane of observation.

Interestingly, the acicular microstructure shows a higher population of 63.26°/[$\overline{10}$ 5 5 $\overline{3}$] boundaries rather than 60°/[1 1 $\overline{2}$ 0] boundaries. This is in line with the results of Beladi et al. [29] on a water quenched Ti-6Al-4V alloy but different to the results of Farabi et al. [14]. The difference in the result of the current work with the predictions in [14] might be due to the fact that their calculation was based on slip being the dominant mechanism accommodating the transformation strain in pure Ti, while martensitic laths also go through twinning during AM of Ti-6Al-4V [44]. The extent to which twinning occurs has been reported to depend on the build height, where for example Tan et al. [44] report numerous twins in samples with 1 mm build height, compared to rare twins observed in a 10 mm sample under the same printing conditions. Moreover, the dominance of 63.26°/[$\overline{10}$ 5 5 $\overline{3}$] boundaries is in line with the calculations of Balachandran et al. [43], demonstrating that they show the minimum elastic interaction energy for coherent α-α boundaries. It appears that during EPBF of Ti-6Al-4V, 63.26°/[$\overline{10}$ 5 5 $\overline{3}$] intervariant boundaries are the favoured boundaries for the as-deposited structures with an acicular morphology. Further pseudo annealing of the microstructure during EPBF, which results in coarsening of the microstructure and a change to colony and basketweave structure, causes preferential growth of the semi-coherent α phase at the expense of coherent areas, shifting the grain boundary population maxima to 60°/[1 1 $\overline{2}$ 0].

The colony microstructure possesses the highest population of 10.53°/[0 0 0 1] boundaries while the acicular microstructure has the lowest volume fraction of these boundaries (Fig. 4). This shows that decreasing the cooling rate increases the number of these boundaries. This might be due to the fact that with lower cooling rates, a larger volume of the α phase forms at the grain boundaries. It has been demonstrated that there is a high tendency for grain boundary α to align its (0 0 0 1) plane to parallel

(1 1 0)$_\beta$ planes in each of the adjacent parent grains [45]. An example of such relationship observed in EPBF Ti-6Al-4V in the current work is shown in Fig. 8. For each (0 0 0 1) orientation, there are two different crystallographically equivalent orientations for the α phase. Impingement of these orientations results in a 10.53°/[0 0 0 1] boundary [45]. Furthermore, Lee et al. [46] have suggested that heterogeneous nucleation of α on the broad face of pre-existing α laths tends to form such 10.53°/[0 0 0 1] boundaries. The other intervariant boundaries (i.e. 60.83°/[$\overline{10}$ $\overline{7}$ 17 3] and 90°/[7 $\overline{17}$ 10 0]) are the crystallographic consequence of impingement of these variant clusters [13]. The colony microstructure also possesses the highest fraction of α-α boundaries that does not correspond to any of the theoretical Burgers OR related intervariant boundaries, while such boundaries are seen less frequently in other microstructures (Fig. 4). This is rationalized considering the higher volume of grain boundary α in the colony microstructure and the fact that non-Burgers OR related boundaries form when α variants inside different β grains impinge at the prior β grain boundary.

A large number of grain boundary phenomena are affected by the grain boundary plane orientation more than the lattice misorientation [20–22,47]. Despite this, there are only a few studies in the literature that have measured the plane distribution for HCP materials. The 2D grain boundary plane distribution (irrespective of misorientation angle/axis) of the studied EPBF Ti-6Al-4V for different microstructures shows a tendency towards prismatic planes and a minimum population for basal planes (Fig. 5). This is in line with previous work on α-Ti [30,31], martensite in pure Ti [14], martensite in Ti-6Al-4V [29], and the AZ31 Mg alloy [48]. It is common in most materials undergoing grain growth for the population of grain boundary planes to be conversely related to the energy [49–51]. There is, however, a lack of data or simulation on the energy of intervariant boundaries in Ti alloys. In some of the limited studies, the energy has been calculated for tilt
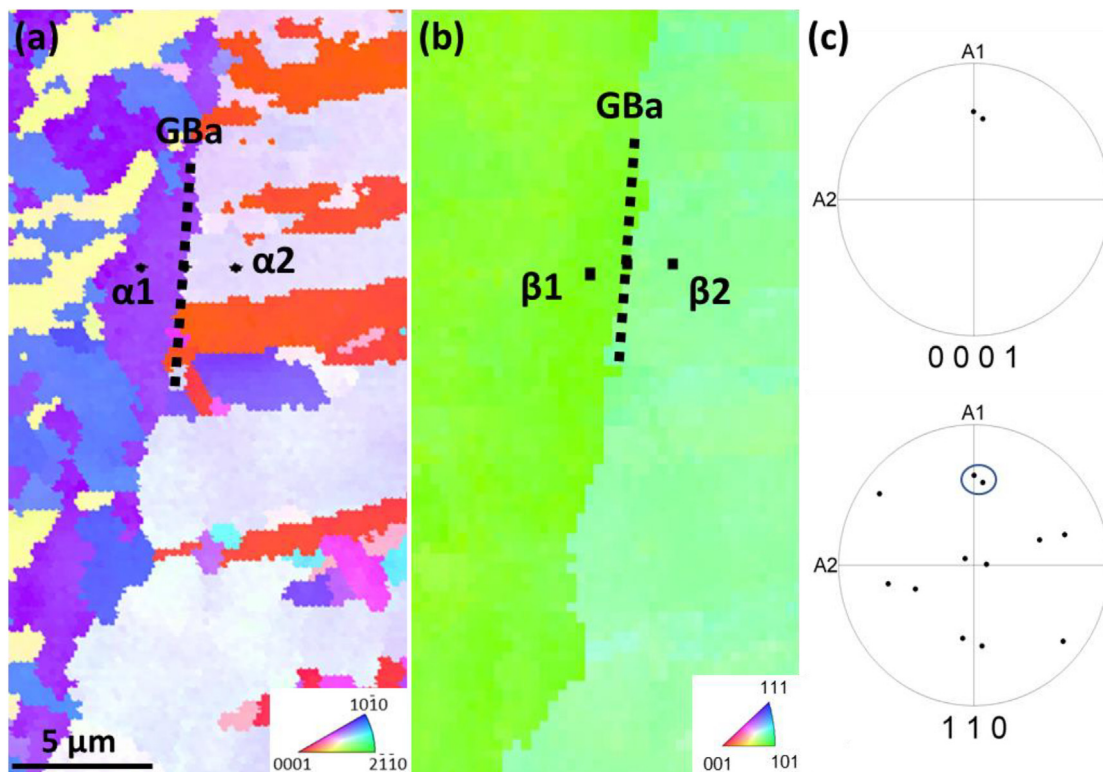
Fig. 8. (a) An IPF map of α grains formed at the prior β grain boundary. (b) The corresponding β map in which β1-β2 boundary is marked by a dashed line. (c) The {0 0 0 1}$_\alpha$ and {110}$_\beta$ and pole figure shows the two α grains are of a low angle deviation and have their basal planes parallel to the β {1 1 0} planes.

boundaries and at 0 K only [52] which might not be applicable to the α phase boundaries in the current work that forms at elevated temperatures.

An alternative, simplified approach is to use interplanar spacing of the planes as a relative measure for the grain boundary energy [53]. It has been shown that a plane with a large interplanar spacing is mostly flat, with only a few broken bonds [53]. This makes such planes match better with the adjacent plane, which results in low repulsion and, in turn, low energy [52]. In Ti-6Al-4V, the interplanar spacing for $(1\,0\,\bar{1}\,0)$, $(1\,1\,\bar{2}\,0)$, $(\bar{1}\,0\,1\,1)$, $(4\,\bar{1}\,\bar{3}\,0)$, and $(0\,0\,0\,1)$ is 0.85 (or 1.70 considering the structure factor [54]), 1.48, 0.36 (or 1.80 considering the structure factor [54]), 0.24 (or 0.47 considering the structure factor [54]), and 2.03 Å, respectively [55]. Based on these values, basal planes are expected to be the most highly populated planes. This contradicts our results and implies that the grain boundary plane distribution in EPBF Ti-6Al-4V, irrespective of the microstructure formed, does not follow a reverse relationship with the energy. The crystallographic constraints imposed by the Burgers OR, instead, determines the plane characteristics. In an ideal Burgers OR, the $(0\,0\,0\,1)_{\alpha}$ plane matches the $(1\,1\,0)_{\beta}$. Such BCC to HCP transformation constraints results in two adjacent α laths to impinge on their prismatic planes during growth [30]. Similar phase transformation-controlled plane distributions have been previously reported for δ-ferrite to austenite [56] and austenite to martensite [57] phase transformations.

The most highly populated intervariant boundary misorientation for the EPBF Ti-6Al-4 V is 60°/[1 1 $\bar{2}$ 0], found in all microstructures. These boundaries terminate on $(\bar{1}\,1\,0\,1)$ planes with only a few degrees deviation from the twist/symmetric tilt $(\overline{15}\,15\,0\,16)$ plane. The $(\bar{1}\,1\,0\,1)$ pyramidal plane has a relatively large interplanar spacing (i.e., 1.80 Å), therefore it is expected to be of low energy. This has been also shown by Wang et al. [52] using molecular dynamic simulations, in which $(\bar{1}\,1\,0\,1)$ plane was found to have the lowest energy ($\sim$169 mJ/m^2) among the [1 1 $\bar{2}$ 0] tilt boundaries. This implies that the triangular clusters of α phase not only minimize the BCC to HCP phase transformation strain, but also result in a minimum plane energy configuration.

5. Conclusions

In the current study, the microstructures and the five-parameter crystallographic characteristics of α-α boundaries in Ti-6Al-4V processed by electron beam powder bed fusion additive manufacturing were studied. The scanning strategy and the distance from the substrate can significantly change the microstructure and α phase morphology in an EPBF Ti-6Al-4V. With an increase in the cooling rate during β to α transformation, there is refinement and a gradual transition from colony to basketweave and acicular morphologies of the α phase. With regards to the intervariant boundaries, the following conclusions can be drawn:

1. Irrespective of their morphology, there is a strict Burgers OR between the α phase with its β parent grain. Colony and basketweave show a significant population of 60°/[1 1 $\bar{2}$ 0] intervariant boundaries, while acicular microstructure shows a maximum at the 63.26°/[$\overline{10}$ 5 5 $\bar{3}$] boundaries.

2. The tendency of intervariant boundaries towards 60°/[1 1 $\bar{2}$ 0] or 63.26°/[$\overline{10}$ 5 5 $\bar{3}$] appears to be closely related to the mechanism of the initial martensitic phase transformation (whether it is accompanied by twinning or slip) and the degree to which α plates are coherent or become semi-coherent during growth induced by pseudo annealing effect in AM.

3. EPBF Ti-6Al-4V microstructure shows a maximum population of prismatic planes and a minimum population of basal planes. This contrasts with the expected inverse relationship between the plane energy and the plane population.

4. The crystallographic constraints imposed by the Burgers OR determines the plane characteristics. In an ideal Burgers OR, the $(0\,0\,0\,1)_{\alpha}$ plane matches the $(1\,1\,0)_{\beta}$. The BCC to HCP transformation constraints result in two adjacent α laths to impinge on their prismatic planes during growth.

5. The 60°/[1 1 $\bar{2}$ 0] intervariant boundaries terminate on $(\bar{1}\,1\,0\,1)$ pyramidal planes that have a relatively large interplanar spacing and a relatively low energy. This implies that the triangular clusters of α phase not only minimizes the BCC to HCP phase transformation strain, but also result in a minimum plane energy configuration.

Declaration of Competing Interest

The authors declare that they have no known competing financial interests or personal relationships that could have appeared to influence the work reported in this paper.

References

[1] C. Leyens, M. Peters (Eds.), Titanium and Titanium Alloys: Fundamentals and Applications, John Wiley & Sons, 2003.

[2] M.J. Donachie, Titanium: A Technical Guide, 2nd Edition ASM International, Materials Park, OH, 2000.

[3] S. Liu, Y.C. Shin, Additive manufacturing of Ti6Al4V alloy: a review, Mater. Des. 164 (2019) 107552.

[4] P. Edwards, A. O'conner, M. Ramulu, Electron beam additive manufacturing of titanium components: properties and performance, J. Manuf. Sci. Eng. 135 (6) (2013).

[5] L.E. Murr, S.M. Gaytan, D.A. Ramirez, E. Martinez, J. Hernandez, K.N. Amato, P.W. Shindo, F.R. Medina, R.B. Wicker, Metal fabrication by additive manufacturing using laser and electron beam melting technologies, J. Mater. Sci. Technol. 28 (1) (2012) 1–14.

[6] D. Herzog, V. Seyda, E. Wycisk, C. Emmelmann, Additive manufacturing of metals, Acta Mater. 117 (2016) 371–392.

[7] J.P. Oliveira, T.G. Santos, R.M. Miranda, Revisiting fundamental welding concepts to improve additive manufacturing: from theory to practice, Prog. Mater. Sci. 107 (2020) 100590.

[8] J.P. Oliveira, A.D. LaLonde, J. Ma, Processing parameters in laser powder bed fusion metal additive manufacturing, Mater. Des. 193 (2020) 108762.

[9] D. Zhang, D. Qiu, M.A. Gibson, Y. Zheng, H.L. Fraser, D.H. StJohn, M.A. Easton, Additive manufacturing of ultrafine-grained high-strength titanium alloys, Nature 576 (7785) (2019) 91–95.

[10] X. Tan, Y. Kok, Y.J. Tan, M. Descoins, D. Mangelinck, S.B. Tor, K.F. Leong, C.K. Chua, Graded microstructure and mechanical properties of additive manufactured Ti–6Al–4V via electron beam melting, Acta Mater. 97 (2015) 1–16.

[11] L.C. Zhang, Y. Liu, S. Li, Y. Hao, Additive manufacturing of titanium alloys by electron beam melting: a review, Adv. Eng. Mater. 20 (5) (2018) 1700842.

[12] W.G. Burgers, Physica 1 (1934) 561–586.

[13] S.C. Wang, M. Aindow, M.J. Starink, Effect of self-accommodation on α-α boundary populations in pure titanium, Acta Mater. 51 (2003) 2485–2503.

[14] E. Farabi, P.D. Hodgson, G.S. Rohrer, H. Beladi, Five-parameter intervariant boundary characterization of martensite in commercially pure titanium, Acta Mater. 154 (2018) 147–160.

[15] W. Gong, Y. Tomota, Y. Adachi, A.M. Paradowska, J.F. Kelleher, S.Y. Zhang, Acta Mater. 61 (2013) 4142–4154.

[16] N. Stanford, P.S. Bate, Crystallographic variant selection in Ti–6Al–4V, Acta Mater. 52 (17) (2004) 5215–5224.

[17] D. Bhattacharyya, G.B. Viswanathan, R. Denkenberger, D. Furrer, H.L. Fraser, Acta Mater. 51 (2003) 4679–4691.

[18] N. Sridharan, A. Chaudhary, P. Nandwana, S.S. Babu, Texture evolution during laser direct metal deposition of Ti-6Al-4V, JOM 68 (3) (2016) 772–777.

[19] P.L. Stephenson, N. Haghdadi, R. Demott, X.Z. Liao, S.P. Ringer, Sophie primig, effect of scanning strategy on variant selection in additively manufactured Ti-6Al-4V, Add. Manuf. 36 (2020) 101581.

[20] N. Haghdadi, D. Abou-Ras, P. Cizek, P.D. Hodgson, A.D. Rollett, H. Beladi, Austenite-ferrite interface crystallography dependence of sigma phase precipitation using the five-parameter characterization approach, Mater. Lett. 196 (2017) 264–268.

[21] A. Serra, D.J. Bacon, Computer simulation of screw dislocation interactions with twin boundaries in H.C.P. metals, Acta Metall. Mater. 43 (1995) 4465–4481.

[22] A. Serra, D.J. Bacon, R.C. Pond, Twins as barriers to basal slip in hexagonal-close-packed metals Met, Mater. Trans. A 33 (2002) 809–812.

[24] J.P. Simmons, L.F. Drummy, C.A. Bouman, M. De Graef (Eds.), Statistical Methods for Materials Science: The Data Science of Microstructure Characterization, CRC Press, 2019.

[25] G.S. Rohrer, D.M. Saylor, B.E. Dasher, B.L. Adams, A.D. Rollett, P. Wynblatt, The distribution of internal interfaces in polycrystals, Z. Met. 95 (4) (2004) 197–214.

[26] G.S. Rohrer, J. Li, S. Lee, A.D. Rollett, M. Groeber, M.D. Uchic, Deriving grain boundary character distributions and relative grain boundary energies from three-dimensional EBSD data, Mater. Sci. Technol. 26 (2010) 661–669.

[27] H.H. Liu, S. Schmidt, H.F. Poulsen, A. Godfrey, Z.Q. Liu, J.A. Sharon, X. Huang, Three-dimensional orientation mapping in the transmission electron microscope, Science 332 (6031) (2011) 833–834.

[28] B. Lin, Y. Jin, C.M. Hefferan, S.F. Li, J. Lind, R.M. Suter, M. Bernacki, N. Bozzolo, A.D. Rollett, G.S. Rohrer, Observation of annealing twin nucleation at triple lines in nickel during grain growth, Acta Mater. 99 (2015) 63–68.

[29] H. Beladi, Q. Chao, G.S. Rohrer, Variant selection and intervariant crystallographic planes distribution in martensite in a Ti-6Al-4V alloy, Acta Mater. 80 (2014) 478–489.

[30] M.N. Kelly, K. Glowinski, N.T. Nuhfer, G.S. Rohrer, The five parameter grain boundary character distribution of α-Ti determined from three-dimensional orientation data, Acta Mater. 111 (2016) 22–30.

[31] V. Randle, G.S. Rohrer, Y. Hu, Five-parameter grain boundary analysis of a titanium alloy before and after low-temperature annealing, Scr. Mater. 58 (3) (2008) 183–186.

[32] N. Haghdadi, E. Whitelock, B. Lim, H. Chen, X. Liao, S.S. Babu, S.P. Ringer, S. Primig, Multimodal γ′precipitation in Inconel-738 Ni-based superalloy during electron-beam powder bed fusion additive manufacturing, J. Mater. Sci. 55 (2020) 13342–13350.

[33] M.M. Kirka, Y. Lee, D.A. Greeley, A. Okello, M.J. Goin, M.T. Pearce, R.R. Dehoff, Strategy for texture management in metals additive manufacturing, Jom 69 (3) (2017) 523–531.

[34] M.T. Jovanović, S. Tadić, S. Zec, Z. Mišković, I. Bobić, The effect of annealing temperatures and cooling rates on microstructure and mechanical properties of investment cast Ti-6Al-4V alloy, Mater. Des. 27 (3) (2006) 192–199.

[35] A. Morawiec, J. Appl. Crystallogr. 44 (6) (2011) 1152–1156.

[36] P.S. Davies, An Investigation of Microstructure and Texture Evolution in the Near-α Titanium Alloy Timetal 834, Thesis University of Sheffield, 2009.

[37] C.S. Daniel, P.D. Honniball, L. Bradley, M. Preuss, J.Q. da Fonseca, Compounds, A detailed study of texture changes during alpha–beta processing of a zirconium alloy, J. Alloys Compd. 804 (2019) 65–83.

[38] S.S. Al-Bermani, M.L. Blackmore, W. Zhang, I. Todd, The origin of microstructural diversity, texture, and mechanical properties in electron beam melted Ti-6Al-4V, Metall. Mater. Trans. A 41 (13) (2010) 3422–3434.

[39] Y.Z. Wang, N. Ma, Q. Chen, F. Zhang, S.L. Chen, Y.A. Chang, Predicting phase equilibrium, phase transformation, and microstructure evolution in titanium alloys, Jom 57 (9) (2005) 32–39.

[40] H.I. Aaronson, G. Spanos, R.A. Masamura, R.G. Vardiman, D.W. Moon, E.S.K. Menon, M.G. Hall, Sympathetic nucleation: an overview, Mater. Sci. Eng. B 32 (3) (1995) 107–123.

[41] R. Shi, Y. Wang, Variant selection during α precipitation in Ti-6Al-4V under the influence of local stress–a simulation study, Acta Mater. 61 (16) (2013) 6006–6024.

[42] K. Glowinski, A. Morawiec, A toolbox for geometric grain boundary characterization, Proc. 1st Int. Conf. 3D Mater. Sci, Springer, Cham 2012, pp. 119–124.

[43] S. Balachandran, A. Kashiwar, A. Choudhury, D. Banerjee, R. Shi, Y. Wang, On variant distribution and coarsening behavior of the α phase in a metastable β titanium alloy, Acta Mater. 106 (2016) 374–387.

[44] X. Tan, Y. Kok, W.Q. Toh, Y.J. Tan, M. Descoins, D. Mangelinck, S.B. Tor, K.F. Leong, C.K. Chua, Revealing martensitic transformation and α/β interface evolution in electron beam melting three-dimensional-printed Ti-6Al-4V, Sci. Rep. 6 (2016) 26039.

[45] Arjen Kamp, Investigation of Titanium α Plates by EBSD Analysis, Master Thesis Delft University of Technology, 2007.

[46] E. Lee, R. Banerjee, S. Kar, D. Bhattacharyya, H.L. Fraser, Selection of alpha variants during microstructural evolution in alpha/beta titanium alloy, Philos. Mag. 87 (2007) 3615.

[47] R. Jones, V. Randle, G. Owen, Carbide precipitation and grain boundary plane selection in overaged type 316 austenitic stainless steel, Mater. Sci. Eng. A 496 (1–2) (2008) 256–261.

[48] H. Beladi, A. Ghaderi, G.S. Rohrer, Five-parameter grain boundary characterisation of randomly textured AZ31 Mg alloy, Philos. Mag. 100 (2020) 456–466.

[49] E.A. Holm, G.S. Rohrer, S.M. Foiles, A.D. Rollett, H.M. Miller, D.L. Olmsted, Validating computed grain boundary energies in fcc metals using the grain boundary character distribution, Acta Mater. 59 (2011) 5250–5256.

[50] S. Ratanaphan, Y. Yoon, G.S. Rohrer, The five parameter grain boundary character distribution of polycrystalline silicon, J. Mater. Sci. 49 (2014) 4938–4945.

[51] H. Beladi, G.S. Rohrer, The relative grain boundary area and energy distributions in a ferritic steel determined from three-dimensional electron backscatter diffraction maps, Acta Mater. 61 (2013) 1404–1412.

[52] J. Wang, I.J. Beyerlein, Atomic structures of symmetric tilt grain boundaries in hexagonal close packed (hcp) crystals, Model. Simul. Mater. Sci. Eng. 20 (2012) 24002.

[53] D. Wolf, Correlation between structure, energy, and ideal cleavage fracture for symmetrical grain boundaries in fcc metals, J. Mater. Res. 5 (1990) 1708–1730.

[54] Q. Fan, A new method of calculating interplanar spacing: the position-factor method, J. Appl. Crystallogr. 45 (2012) 1303–1308.

[55] E. Farabi, V. Tari, P.D. Hodgson, G.S. Rohrer, H. Beladi, On the grain boundary network characteristics in a martensitic Ti-6Al-4V alloy, J. Mater. Sci. 55 (2020) 15299–15321.

[56] N. Haghdadi, P. Cizek, P.D. Hodgson, V. Tari, G.S. Rohrer, H. Beladi, Effect of ferrite-to-austenite phase transformation path on the interface crystallographic character distributions in a duplex stainless steel, Acta Mater. 145 (2018) 196–209.

[57] H. Beladi, G.S. Rohrer, A.D. Rollett, V. Tari, P.D. Hodgson, The distribution of intervariant crystallographic planes in a lath martensite using five macroscopic parameters, Acta Mater. 63 (2014) 86–98.